Electronic Supplementary Material (ESI) for Lab on a Chip.
This journal is © The Royal Society of Chemistry 2023

Supplementary Information

Metallic Micro-Ring Device for Highly Efficient Large Cargo Delivery in Mammalian Cells using Infrared Light Pulse

Ashwini Shinde[1#], Pallavi Shinde[1#], Srabani Kar[2], Kavitha Illath[1], Souvik Dey[3], Nitish R. Mahapatra[3], Moeto Nagai[4], Tuhin Subhra Santra*[1]

[1]Department of Engineering Design, Indian Institute of Technology Madras, Chennai, India.
[2]Department of Electrical Engineering, University of Cambridge, UK.
[3]Department of Biotechnology, Indian Institute of Technology Madras, Chennai, India.
[4]Department of Mechanical Engineering, Toyohashi University of Technology, Japan.

[#] Authors Contributed Equally; *Corresponding Author: tuhin@iitm.ac.in, santra.tuhin@gmail.com

Table S1: The comparison of TMR structure shape and dimensions with previously reported microstructures.

Shape of microstructure	Structure material, dimension & interspacing	Theoretical study & temperature increment	Cost-effective/ fabrication complexity	Large cargo (Cas9/ enzyme)	Max. cell viability (%)	Max. delivery efficiency (%)	Ref.
Microdisc	Titanium 3 µm diameter 15 µm gap	Yes ~1000 K	Simple design & fabrication	No	100	98	1
Nanodisc	Gold 350 nm, 1, 2, & 10 µm	Yes ~ 650 K	Complex fabrication	No	> 98	> 98	2
Pyramid pit micropore	Chromium/gold 50 µm (side length), 2 µm (pyramid top) 75 µm spacing	No	Not so complex	CRISPR-Cas9 (> 9kbp)	-	> 90	3
Microwell with nanoscale sharp tip	Titanium 8 µm diameter	Yes ~1000 K	Complex fabrication	No	> 96	> 84	4
Tipless pyramid	Gold on the sides and top is polymer 300 nm (aperture), 2.2 µm base length & 1 µm spacing	Yes	Complex fabrication	No	-	-	5
Microring	Titanium 10 µm (outer), 3 µm (inner) &	Yes ~1200 K	Single-step & cost-effective	Yes Enzyme (688	97	96	Present work

	10 µm spacing			kDa)			

1. Shinde, P.; Kar, S.; Loganathan, M.; Chang, H. Y.; Tseng, F.-G.; Nagai, M.; Santra, T. S. Infrared Pulse Laser-Activated Highly E Ffi Cient Intracellular Delivery Using Titanium Microdish Device. *ACS Biomater. Sci. Eng.* **2020**, *6* (10), 5645–5652. https://doi.org/10.1021/acsbiomaterials.0c00785.
2. Zhao, C.; Man, T.; Xu, X.; Yang, Q.; Liu, W.; Jonas, S. J.; Teitell, M. A.; Chiou, P. Y.; Weiss, P. S. Photothermal Intracellular Delivery Using Gold Nanodisk Arrays. *ACS Mater. Lett.* **2020**, *2* (11), 1475–1483. https://doi.org/10.1021/acsmaterialslett.0c00428.
3. Dong, Z.; Jiao, Y.; Xie, B.; Hao, Y.; Wang, P.; Liu, Y.; Shi, J.; Chitrakar, C.; Black, S.; Wang, Y. C.; Lee, L. J.; Li, M.; Fan, Y.; Chang, L. On-Chip Multiplexed Single-Cell Patterning and Controllable Intracellular Delivery. *Microsystems Nanoeng.* **2020**, *6* (1), 1–11. https://doi.org/10.1038/s41378-019-0112-z.
4. Man, T.; Zhu, X.; Chow, Y. T.; Dawson, E. R.; Wen, X.; Patananan, A. N.; Liu, T. L.; Zhao, C.; Wu, C.; Hong, J. S.; Chung, P. S.; Clemens, D. L.; Lee, B. Y.; Weiss, P. S.; Teitell, M. A.; Chiou, P. Y. Intracellular Photothermal Delivery for Suspension Cells Using Sharp Nanoscale Tips in Microwells. *ACS Nano* **2019**, *13* (9), 10835–10844. https://doi.org/10.1021/acsnano.9b06025.
5. Courvoisier, S.; Saklayen, N.; Huber, M.; Chen, J.; Diebold, E. D.; Bonacina, L.; Wolf, J. P.; Mazur, E. Plasmonic Tipless Pyramid Arrays for Cell Poration. *Nano Lett.* **2015**, *15* (7), 4461–4466. https://doi.org/10.1021/acs.nanolett.5b01697.

COMSOL Simulation Details

The simulation was conducted in a 2D axis symmetry configuration, with the model's symmetry in the Z-direction. The Electromagnetic Waves, Frequency Domain (emw) module was used to calculate resistive heating, which is assumed to be the source of local heating and temperature rise. To get temporal and spatial temperature changes, we created two temperature models (details are supplied in the main paper) that are solved using the COMSOL partial differential equations module. The parameters used in the simulation are mentioned in the table below.

Table S2: List of parameters for COMSOL Simulation

Radius of the disc	1500 nm
Thickness of disc	150 nm
Electron heat capacity coefficient, α	328.9 J $m^{-3}K^{-2}$, Ref[1]
Mass density of Titanium, ρ_{Ti}	4506 kg/m[2]
Electron thermal conductivity, k_e	15.3 W/m.K, Ref[3]
Lattice thermal conductivity, k_l	5.2 W/m.K, Ref[3]
Lattice heat capacity, C_l	2.3×10^6 J/m^3K, Ref [4]
Electron-lattice coupling coefficient, g	15×10^{17} W/m^3K, Ref [1]

Mass density of water, ρ_w	1000 kg/m^3
Heat capacity of water, C_w	4182 J/kg.K
Thermal conductivity of water, k_w	0.6 W/m.K
Thermal conductivity at Ti/water interface, g_w	105×10^6 W/m^{2}K, calculated following Ref [5]
Mass density of SiO_2 substrate, ρ_s	2230 kg/m^3 Ref [6]
Heat capacity of substrate, Cs	830 J/kg.K Ref [6]
Thermal conductivity of substrate, k_s	1.2 W/m.K Ref [6]
Thermal conductivity at Ti/substrate interface, g_s	1725×10^6 W/m^{2}K; calculated following Ref [5]
Thermal conductivity at substrate/water interface, g_{sw}	65.8×10^8 W/m^{2}K; calculated following Ref [5]

1. Z. Lin, L. V. Zhigilei, V. Celli, Electron-phonon coupling and electron heat capacity of metals under conditions of strong electron-phonon nonequilibrium, Phys. Rev. B - Condens. Matter Mater. Phys. 77 (2008) 1–17. https://doi.org/10.1103/PhysRevB.77.075133.
2. T. Bell, Titanium Properties and Characteristics, ThoughtCo. (2020). https://www.thoughtco.com/metal-profile-titanium-2340158.
3. R.W. Powell, R.P. Tye, The thermal and electrical conductivity of titanium and its alloys, J. Less-Commn Met. 3 (1961) 226–233.
4. R.R. Rao, A. Rajput, Lattice specific heat and thermal expansion of titanium, Phys. Rev. B. 19 (1979) 3323–3328. https://doi.org/10.1103/PhysRevB.19.3323.
5. G. Chang, F. Sun, J. Duan, Z. Che, X. Wang, J. Wang, M.J. Kim, H. Zhang, Effect of Ti interlayer on interfacial thermal conductance between Cu and diamond, Acta Mater. 160 (2018) 235–246. https://doi.org/10.1016/j.actamat.2018.09.004.
6. BOROFLOAT® 33, Thermal Properties, (n.d.).

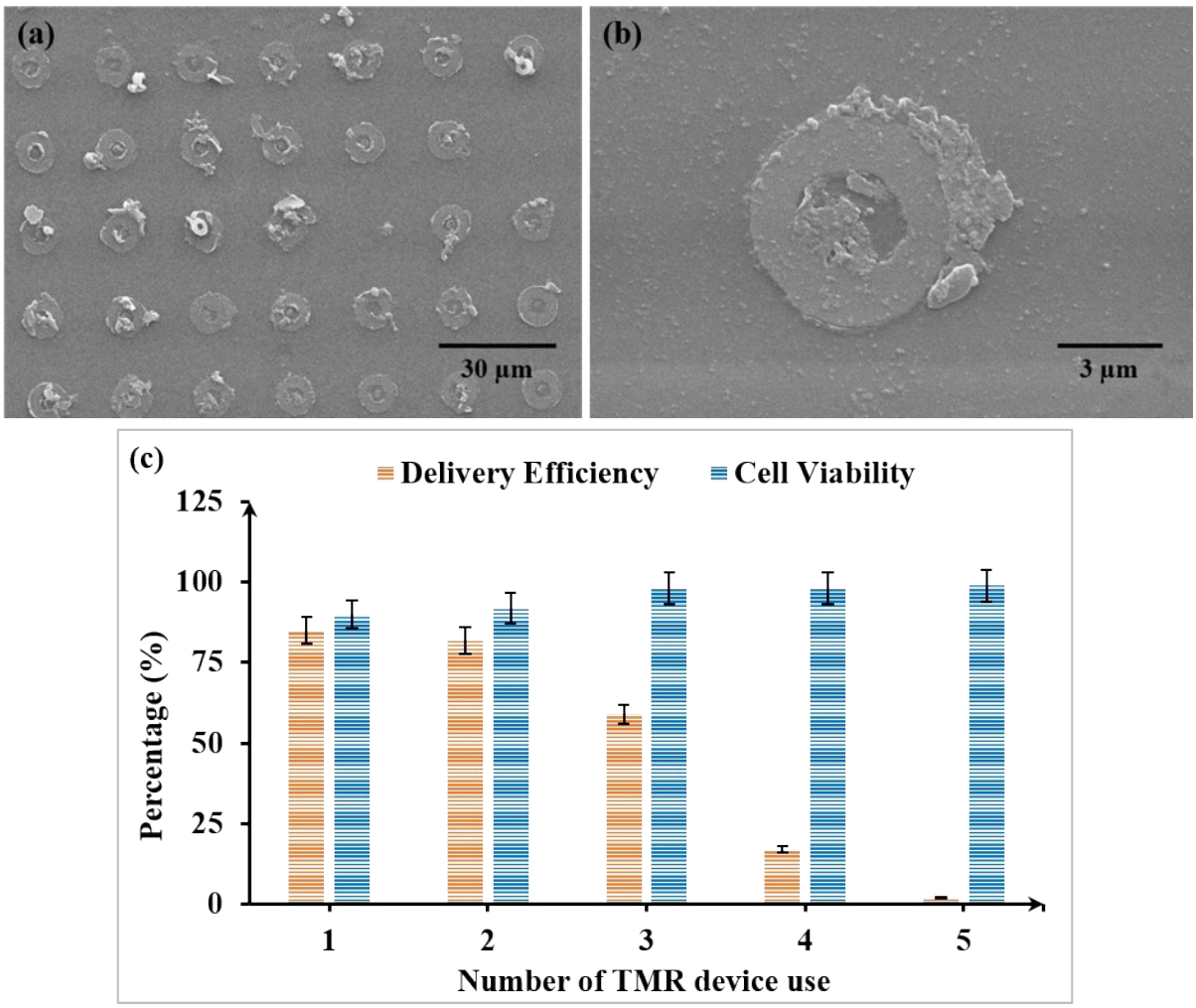

Figure S1: (a, b) Scanning electron microscopy (SEM) image of TMR device after three times photoporation experiment with laser fluence of 45 mJ/cm^2 at 1050nm for 300 pulses. (c) Quantification of delivery efficiency and cell viability after BG enzyme delivery into L929 cells using same TMR device five times with laser fluence of 45 mJ/cm^2 at 1050nm for 250 pulses (n=3 independent experiments, data presented as mean ± S.D.).

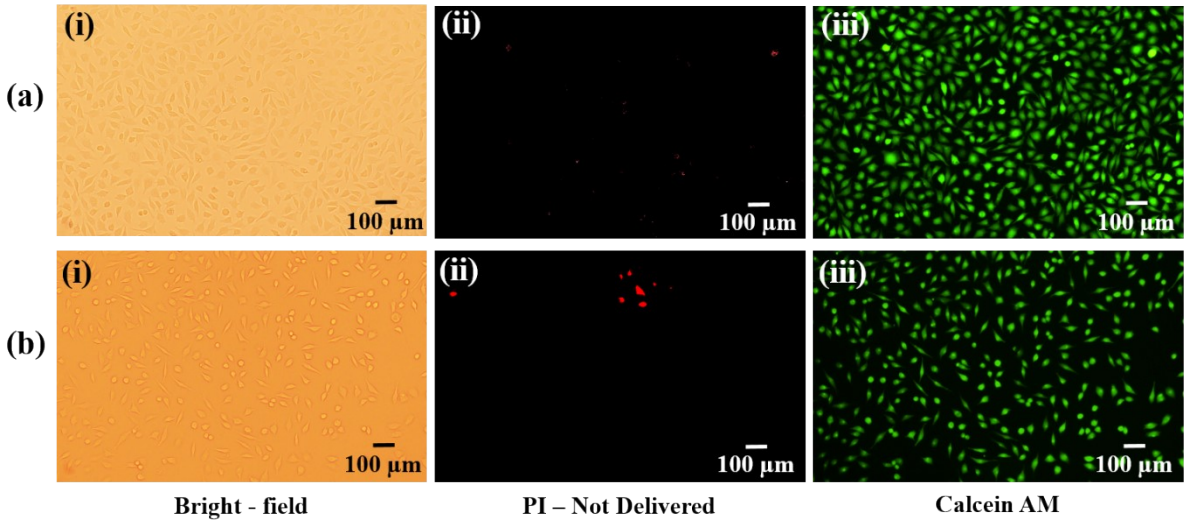

Figure S2. Control experiment on L929 cells (Olympus microscope laser exposure for 100 ms) – (a) With TMR platform and no laser exposure- (i) bright-field image; (ii) PI dye staining on the nucleus of dead cells; (iii) cell viability test using calcein-AM confirmed that almost all cells are live (green color). (b) Without TMR platform and with laser exposure at 45 mJ/cm2 for 250 pulses - (i) bright-field image; (ii) PI dye staining on the nucleus of dead cells; (iii) cell viability test using calcein-AM confirmed that almost all cells are live (green color).

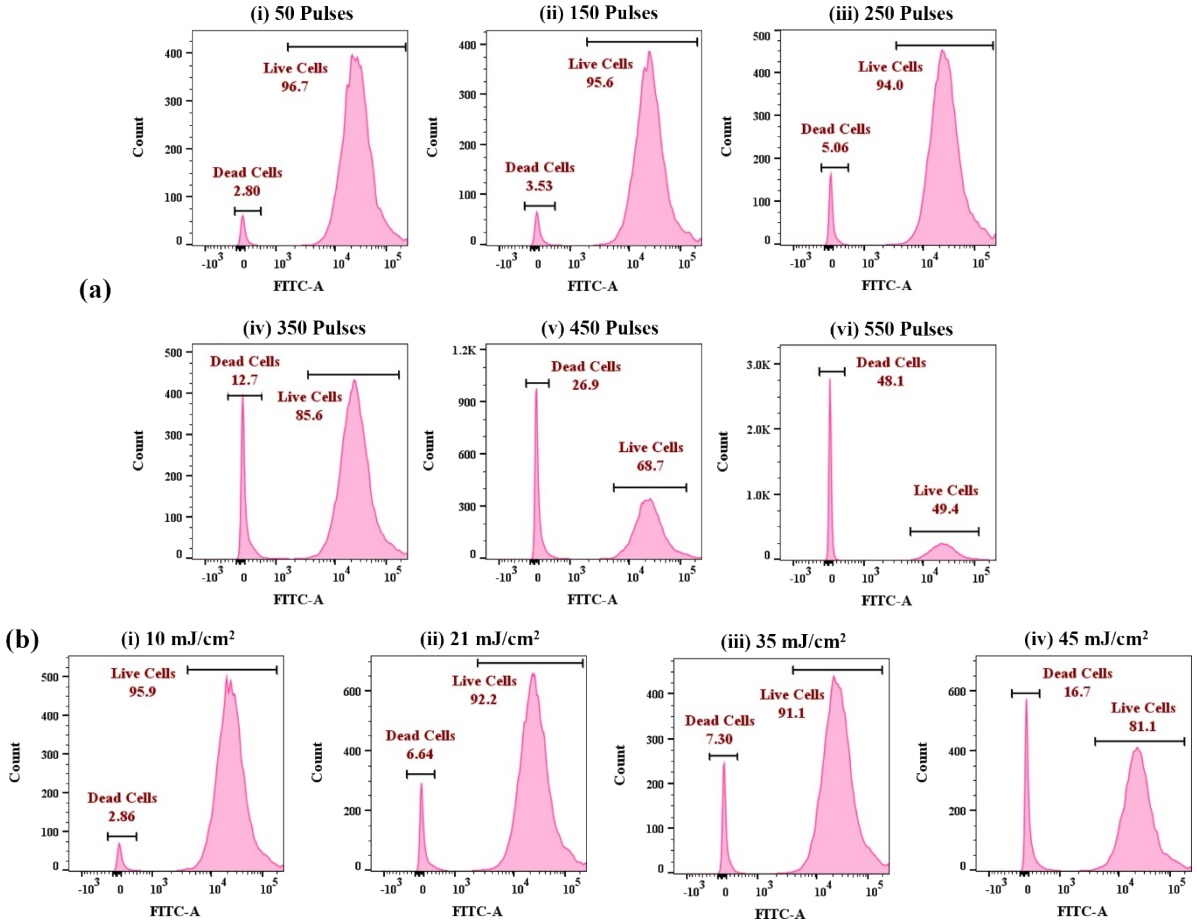

Figure S3: Flow cytometry-based assessment for live and dead cells by – (a) Varying number of pulses at fluence 21 mJ/cm² – (i) 50 pulses; (ii) 150 pulses; (iii) 250 pulses; (iv) 350 pulses; (v) 450 pulses; (vi) 550 pulses. (b) Varying fluence of the pulse laser for 250 pulses – (i) 10 mJ/cm²; (ii) 21 mJ/cm²; (iii) 35 mJ/cm²; (iv) 45 mJ/cm².

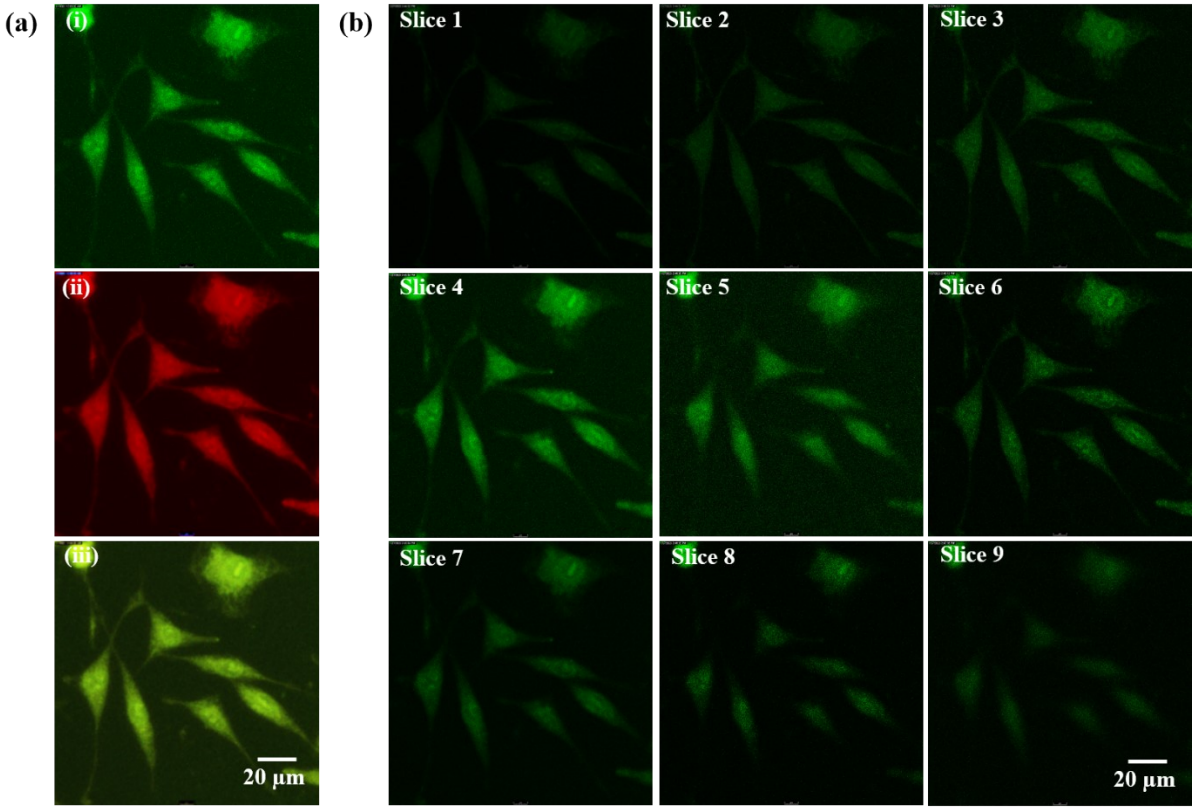

Figure S4: Confocal microscope image of L929 cells after siRNA-6FAM delivery using TMR-mediated optoporation (Confocal microscope pin hole used 1.0 with laser intensity at 1.01 mW). (a) Maximum intensity projection images of – (i) siRNA-6FAM (green) delivery; (ii) Calcein red-orange AM (red) showing the viability of cells after siRNA delivery; (iii) merge (green to yellowish green) images of Calcein red-orange AM and siRNA-6FAM confirmed live cells after delivery (n=3). (b) Split Z - stack images for the optoporated images of siRNA-6FAM delivery (Slice 1 to Slice 9).

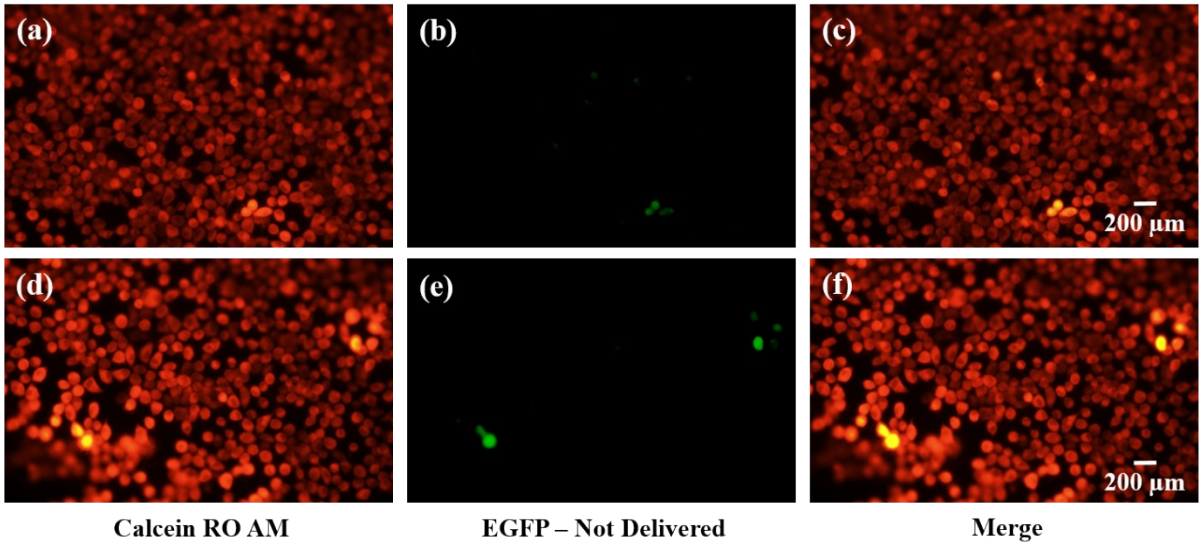

Figure S5: Control experiment on N2a cells (Olympus microscope laser exposure for 1 sec) – (a) With TMR platform and no laser exposure- (i) Calcein red-orange AM for live cells; (ii) EGFP showing not delivered;

(iii) merge image showing live cells with no EGFP delivery. (b) Without TMR platform and with laser exposure at 45 mJ/cm^2 for 250 pulses - (i) Calcein red-orange AM for live cells; (ii) EGFP showing not delivered; (iii) merge image showing live cells with no EGFP delivery.

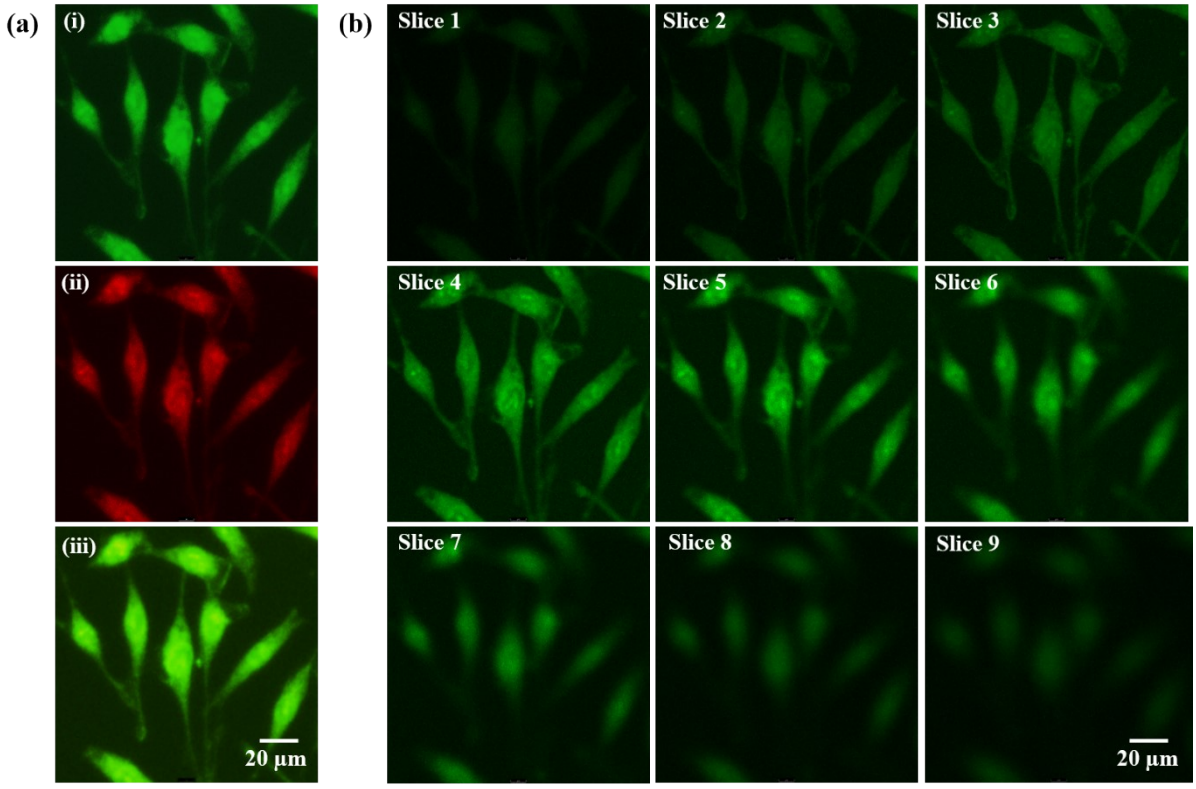

Figure S6: Confocal microscope image of L929 cells after EGFP delivery using TMR-mediated optoporation (Confocal microscope pin hole used 1.0 with laser intensity at 1.01 mW). (a) Maximum intensity projection images of – (i) EGFP (green) delivery; (ii) Calcein red-orange AM (red) showing the viability of cells after EGFP delivery; (iii) merge (green to yellowish green) images of Calcein red-orange AM and EGFP confirmed live cells after delivery (n=3). (b) Split Z - stack images for the optoporated images of EGFP delivery (Slice 1 to Slice 9).

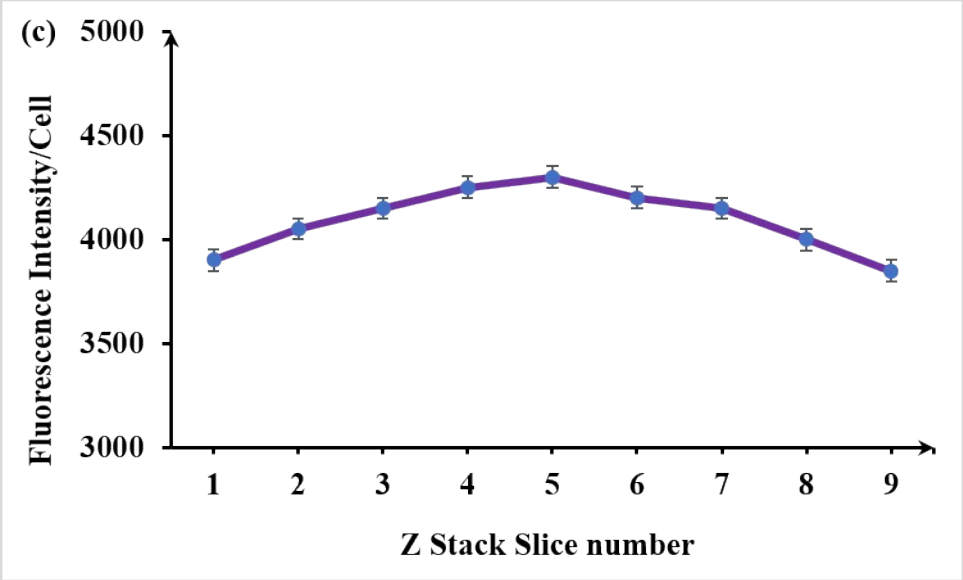

Figure S7: Quantification of fluorescence intensity of merged images on a per cell basis indicating uniform delivery and viability of cells (n=3 independent experiments, data presented as mean ± S.D).

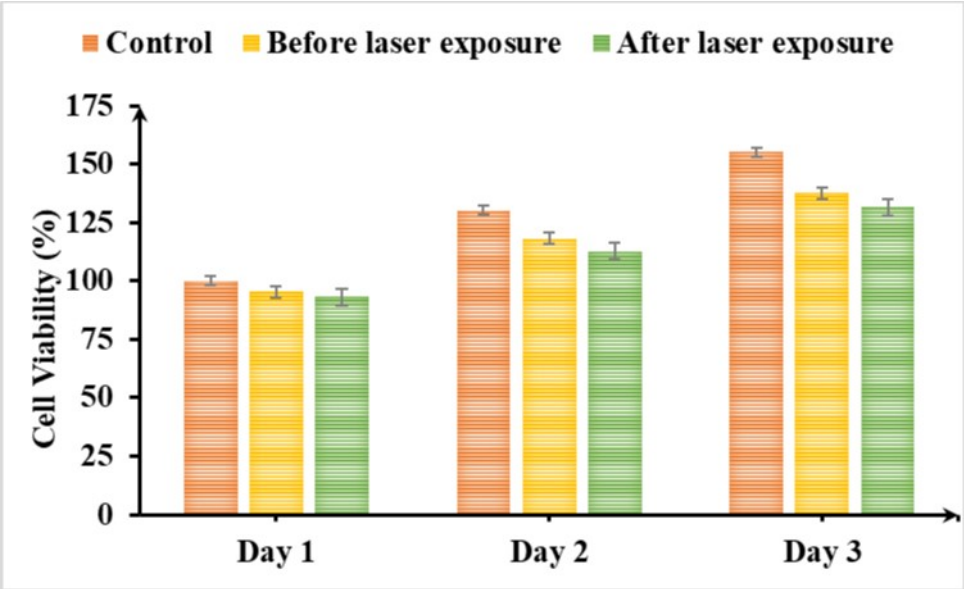

Figure S8: Cell viability of SiHa cells using MTT assay on different days after laser exposure with wavelength at 1050 nm, fluence of 21 mJ/cm^2, and 250 pulses.